Nanoscale

PAPER

View Article Online
View Journal | View Issue

Cite this: *Nanoscale*, 2026, **18**, 3651

Thermoelectrochemistry-enabled phase and morphology control of metal phosphide nanocrystals

Hyokyum Ahn, Yunwoo Nam, Taeyeon Kang and Hyun S. Ahn *

Received 12th November 2025,
Accepted 9th January 2026

DOI: 10.1039/d5nr04780c

rsc.li/nanoscale

Precise control over nanocrystal morphology remains a challenge in direct electrochemical synthesis of transition metal phosphides (TMPs), typically requiring post-synthetic thermal treatment. This study exploits selective surface heating during electrochemical synthesis to overcome kinetic barriers for crystallization, enabling the preparation of highly ordered cobalt and nickel phosphide nanostructures. Systematic voltage modulation yielded Co_2P nanostructures with controlled morphologies including single nanorods, branched rods, and bundled rods with tunable dimensions and facet orientation. Extension to nickel precursors produced Ni_2P with octahedral and plate-like morphologies, suggesting the generalizability of this approach. Electrochemical characterization unveiled important structure–activity relationships: Co_2P nanorod bundles exhibiting superior electrocatalysis (for both hydrogen and oxygen evolution reactions) compared to single nanorods, owing to the overexpressed active facets. This straightforward electrochemical synthetic platform enables rational design of catalysts through direct morphological engineering without complex post-treatment and is readily extensible to other transition metal compounds.

1. Introduction

The realization of renewable energy technologies, such as water electrolyzers and fuel cells, hinges upon the development of high-performance electrocatalysts.[1–3] Platinum group metal-based catalysts are the best known examples; however, their widespread adoption is impeded by high costs and material scarcity.[4–6] Consequently, there is an urgent demand for Earth-abundant and inexpensive alternatives based on non-precious metals.[2,7,8]

Among these, transition metal phosphides (TMPs) have emerged as promising candidates, owing to their elemental abundance, tunable electronic structures, and exceptional electrochemical activity.[9–12] Nevertheless, conventional synthetic approaches, such as solvothermal or phosphidation reactions, inherently suffer from drawbacks including impurity incorporation, reliance on costly and complex equipment, and the need for post-synthetic treatment.[9,13–16]

In contrast, electrochemical synthesis enables catalyst fabrication in the absence of chemical reductants, leveraging low energy and streamlined processes.[17–20] Despite these advantages, successful direct synthesis of TMPs with high crystallinity or controlled morphologies remains rare, and post-treatment steps (*e.g.*, thermal annealing) have been customarily indispensable.[20–22] In our previous work, we demonstrated selective surface heating in electrochemical syntheses, achieving localized temperatures exceeding electrolyte boiling points at the electrode surface, which facilitated the synthesis of single-crystalline nanoparticles.[23]

In this study, we exploit surface-localized thermoelectrochemistry to finely control the nanostructure morphologies of transition metal phosphides (cobalt and nickel) and evaluate their intrinsic electrocatalytic properties. By modulating the applied voltage sequence, we synthesized diverse Co_2P morphologies from single nanorods to bundled rods while enabling fine tuning of particle shape, dimension, and aspect ratio. This approach strategically exposes catalytic active sites, enhancing selectivity and activity and was equally effective for tailoring the growth of nickel phosphides. Beyond TMPs, this methodology can be readily extendable to the syntheses of a variety of metal-main group compounds.

2. Experimental

2.1. Synthesis

2.1.1. Electrochemical cell and surface-heating reactor design. A custom cell architecture was constructed to facilitate selective thermal contact (Scheme 1). Glassy carbon substrates were affixed to a Teflon-based cell using Teflon and Kapton

Department of Chemistry, Yonsei University, Seoul, 03722, Republic of Korea.
E-mail: ahnhs@yonsei.ac.kr

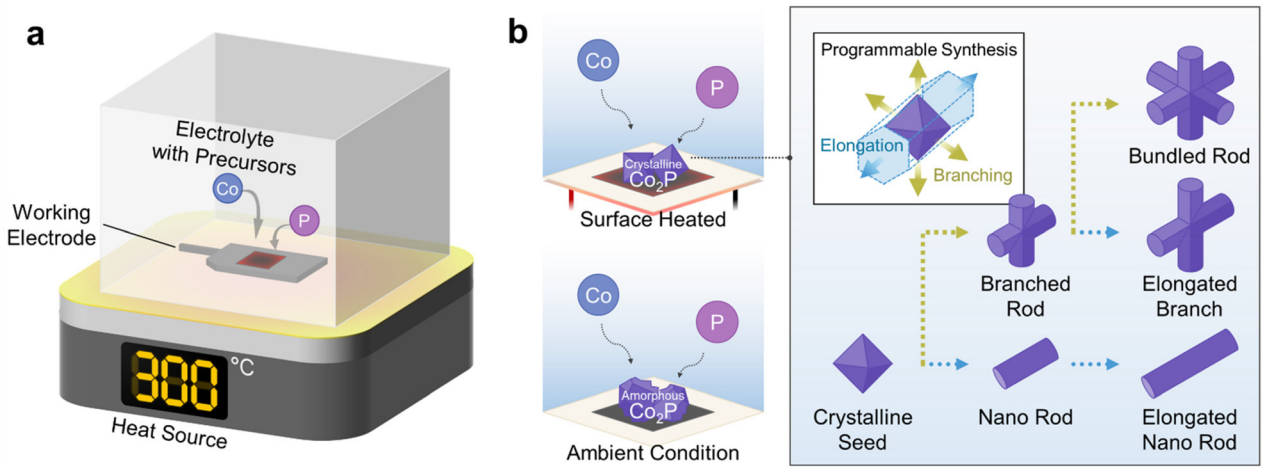

Scheme 1 Schematic illustration of the surface-heated electrochemical cell enabling direct synthesis and morphology control of transition metal phosphide nanostructures.

tape. The assembly was maintained on a hotplate at a target temperature of 300 °C throughout the experiment. Under operation, the glassy carbon substrate was confirmed to reach a maximum temperature of 285 °C. Based on COMSOL modelling,[23] the electrode surface temperature in solution reached approximately 260 °C, while thermometer measurements confirmed that the bulk electrolyte remained at 85–95 °C during deposition, thereby maintaining the desired thermal gradient.

2.1.2. Solution composition and variables. Deionized water was prepared using the Youngin Instruments Aquapuri 5 water purification system (18.2 MΩ cm, 3 ppb total oxidizable carbon). Sodium nitrate ($NaNO_3$ ≥ 99.0%) and sodium hypophosphite monohydrate (NaH_2PO_2 ≥ 99%) were obtained from Sigma-Aldrich and used as received. Cobalt(II) nitrate hexahydrate ($Co(NO_3)_2$ ≥ 99%) and boric acid (H_3BO_3 99.6%) were obtained from Thermos Scientific and used as received.

The electrolyte consisted of 1 M $NaNO_3$ and 0.15 M H_3BO_3, while the precursors were 0.1 mM $Co(NO_3)_2$ and 5 M NaH_2PO_2. The molar ratios of each component were systematically screened and optimized based on compositional and morphological changes. For instance, under cobalt-rich conditions (Co : P = 100 mM : 1 M), the formation of hexagonal closed packed cobalt (hcp-Co) crystals was observed.[24–27] However, increasing P ratios led to the emergence of polycrystalline spherical morphologies. However, even at Co : P = 2 : 1, clear facet formation was not identified (Fig. S1 and S2).

2.1.3. Synthesis conditions. Electrochemical synthesis was performed using a DY2300 potentiostat. Glassy carbon was employed as the working electrode, $Ag/AgNO_3$ (double junction) as the reference electrode, and platinum wire as the counter electrode. Linear sweep voltammetry was conducted over a potential window of −0.76 V to −1.25 V, with growth control achieved by holding specific step potentials (E step) for designated durations (t step). This cycle was repeated 40 times. A comparative set of experiments was conducted at ambient temperature (25 °C) to evaluate thermal effects on nanostructure formation.

2.2. Characterization

Morphological, compositional, and crystallographic properties of the nanostructures were comprehensively evaluated using scanning electron microscopy (SEM), transmission electron microscopy (TEM), EDS, high-resolution TEM (HR-TEM), and selected area electron diffraction (SAED) analyses. SEM (JEOL, JSM 7610f-plus) was used for observing the surface morphology of metal nanoparticles. TEM was performed using a JEM-F200 (JEOL) for imaging metal nanoparticles and diffraction patterns. For TEM measurement, metal nanoparticles were attached to TEM grids by rubbing. TEM grids with pure carbon on copper grids were purchased from Ted Pella, Inc. Electrochemical analysis was performed using a DY2300 potentiostat, with 0.5 M H_2SO_4 (98% DAEJUNG) solution and 1 M KOH (99.99% Sigma-Aldrich) solution. In acid solution, the reference electrode was Ag/AgCl and in base solution, the reference electrode was Hg/HgO.

3. Results and discussion

3.1. Thermoelectrochemical deposition of nanostructures

Co_2P synthesized at ambient temperature predominantly exhibited polycrystalline or amorphous morphologies (Fig. S3). This is attributed to insufficient activation energy for crystal lattice formation, consistent with reports on solvothermal synthesis.[16,27,28]

Upon application of surface heating, locally elevated temperatures (300 °C) facilitated the formation of single-crystal nanostructures, including nanorods, branched rods, and nanorod bundles (Fig. 1a–c). Elemental mapping by TEM-EDS confirmed a homogeneous Co : P ratio of 2 : 1 for the syn-

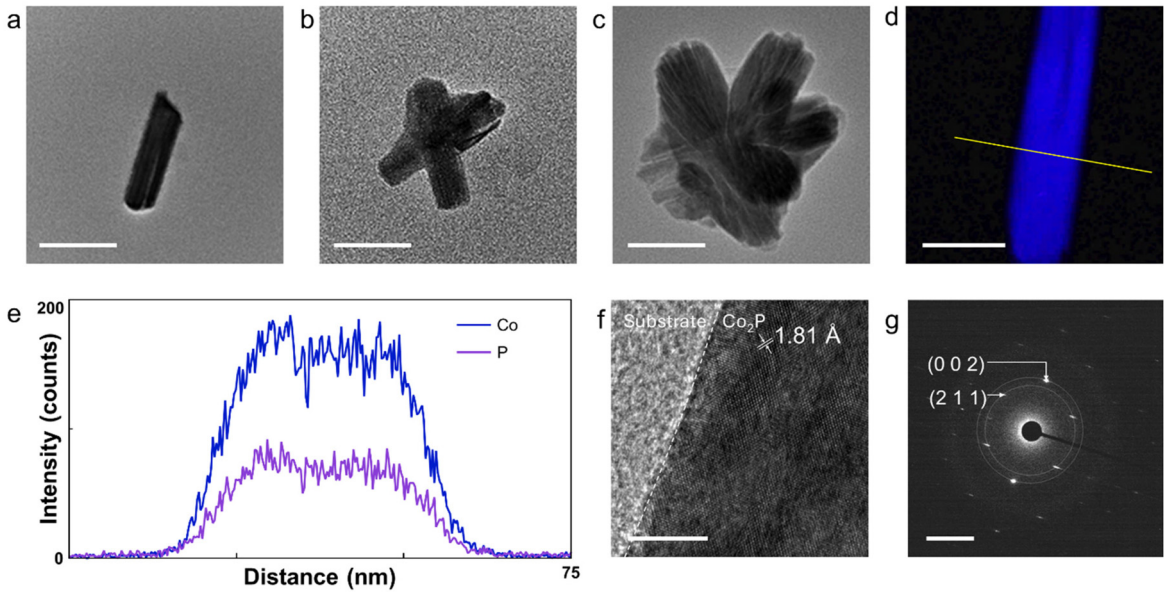

Fig. 1 (a–c) Representative TEM images of Co_2P nanostructures with different morphologies. (a) Nanorod-type particles, (b) branched rod particles exhibiting a single branch, and (c) bundle rod particles. Scale bars for panels a–d correspond to 50 nm. (d) EDS mapping reveals the elemental distribution of Co and P, confirming the homogenous composition. (e) Line scan EDS analysis along the rod axis indicates a uniform Co : P atomic ratio. (f) HR-TEM image of the rod-type nanostructure, identifying lattice fringes consistent with characteristic *d*-spacing values for Co_2P. Scale bars for panel F correspond to 5 nm; (g) SAED pattern of the same specimen matches well with the reference Co_2P, confirming phase purity and crystallinity.

thesized nanostructures (Fig. 1d, e and Fig. S4). The corresponding HR-TEM analysis revealed a single-phase Co_2P with a measured lattice fringe spacing (*d*-spacing) of 1.81 Å, in agreement with literature values. Furthermore, SAED patterns exhibited diffraction spots corresponding to the (002) and (211) crystallographic planes of Co_2P (ICDD card # 00-032-0306 for Co_2P), indicative of single-crystal domains (Fig. 1f and g).[29]

These results demonstrate that thermoelectrochemistry enabled the climb over the energy barriers for crystal lattice formation.[23] This mechanism closely parallels the surface energy-driven crystal growth processes observed in conventional syntheses.[27,28]

3.2. Growth and etching behaviour under different voltage profiles and precise morphology control by programmed thermoelectrolysis

Based on time–current graphs and applied voltage sequences, the growth directionality and morphology were precisely controlled through modulation of the designated step voltage (E step) and hold time (t step) (Fig. 2a–c). As depicted in Fig. 2, the thermoelectrochemical deposition potential window can be divided into three regimes: (1) (the etching zone) potential window of −0.95 V to −1.0 V revealed transient anodic currents indicative of etching (Fig. S5), (2) (the elongation zone) beyond −1.04 V, increasing cathodic currents promoted nanorod growth, and (3) (the branching zone) at potentials exceeding −1.1 V, branching and bundling of the nanorods became prevalent, presumably due to additional seeding and growth point introduction along an established rod.

Varying the E step yielded controlled branching and bundling of the nanorods (Fig. 2a–f). As the E step shifted more cathodically, the resultant morphology transitioned from nanorods to branched rods and ultimately to nanorod bundles. This evolution correlates with the distribution of reduction sites on the particle surface; at higher overpotentials, reduction occurs uniformly across all facets, while at lower overpotentials, reduction is localized preferentially to specific facets.

Remarkably, the length of the single nanorods, therefore the aspect ratio of the material, was precisely tunable by simple modulation of the holding time at the elongation potentials. Increasing the t step lengthened the nanorods (in the range of 25 to 200 nm), while the width remained relatively constant between 24 and 30 nm. Statistical analysis *via* histogram plotting of 100 particles quantitatively assessed the size distribution and growth trends (Fig. 2h). This fine voltage modulation exerted substantial influence on both growth kinetics and the resultant Co_2P particle morphology. Facile preparation of phase pure and crystalline single nanorods with a tunable aspect ratio is particularly attractive for many applications, including electrocatalysis (*vide infra*).

3.3. Extension to other metal phosphides

The surface-heating electrochemical synthesis protocol was applied to nickel-based precursors yielding octahedral and plate-like growth patterns (Fig. 3a and Fig. S6). EDS analysis confirmed compositional ratios consistent with the Ni_2P stoichiometry (Fig. 3b and c). HR-TEM analysis revealed a *d*-spacing value of 1.61 Å, corresponding to the Ni_2P (300) crys-

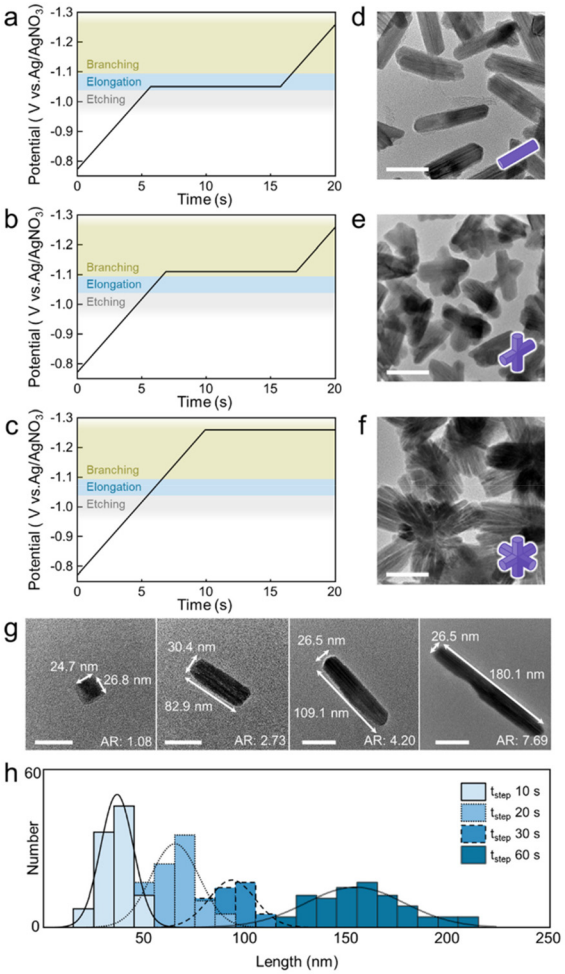

Fig. 2 (a–c) Voltage profiles illustrating the stepwise changes in applied potential (E step) during the synthesis process. (d–f) TEM images of Co_2P nanostructures synthesized under the corresponding voltage conditions shown in a–c; nanorod (a), branched rods (b), and bundled rods (c) morphologies. (g) TEM images of samples synthesized by varying the voltage hold time (t step) under condition A, with the corresponding aspect ratios (length/width) for each sample. (h) Histogram presenting the length distribution of 100 nanorods obtained in (g), quantitatively evaluating the growth trends and size distribution of Co_2P nanorods as a function of t step. All TEM images feature a scale bar of 50 nm.

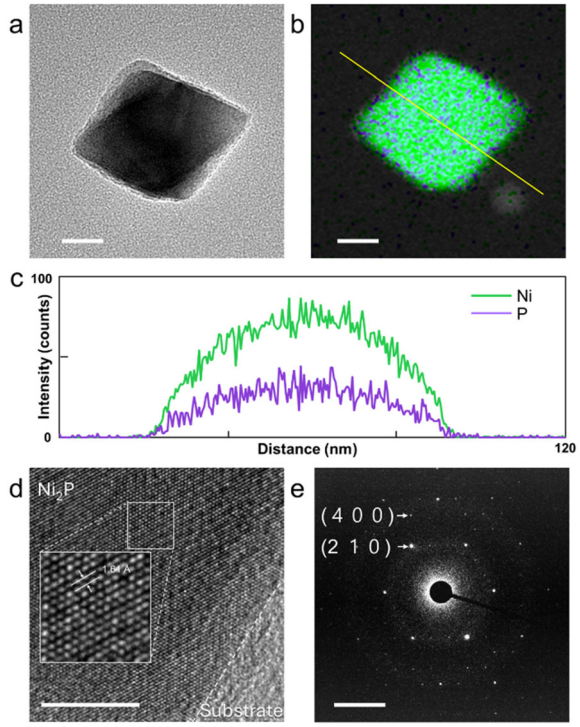

Fig. 3 (a) TEM image of a representative Ni_2P nanostructure showing an octahedral-like morphology synthesized. (b) Elemental EDS mapping image confirming the homogeneous distribution of nickel and phosphorus across the particle. (c) EDS line scan profile along the particle axis, verifying a Ni : P atomic ratio consistent with the Ni_2P stoichiometry. (d) HR-TEM image identifying lattice fringes with a *d*-spacing of 1.61 Å, corresponding to the (300) plane of Ni_2P. (e) SAED pattern exhibiting diffraction reflections matching the (400) and (210) planes of Ni_2P, confirming the phase purity and crystallinity. Scale bars are a and b image 50 nm, d 5 nm and e 1/5 nm.

tallographic plane (ICDD card # 00-003-0953).[30] Additionally, SAED patterns exhibited well-defined reflections matching the (400) and (210) planes of Ni_2P (Fig. 3d and e). These results experimentally validate that the synthesis strategy reported here is not limited to the Co–P system but can be readily extended to diverse transition metal phosphides and alloy systems.

3.4. Electrocatalysis of Co_2P nanorods

The catalytic activities of the thermoelectrochemically prepared Co_2P nanorods were evaluated for the hydrogen evolution reaction (HER) and oxygen evolution reaction (OER) in both acidic and alkaline electrolytes. To ensure a fair comparison accounting for differences in active surface areas, all polarization curves were normalized by the electrochemically active surface area (ECSA) measured using the non-faradaic capacitance (Fig. S7 and Fig. S8).

3.4.1. Hydrogen evolution reaction (HER) activity. Fig. 4a presents the ECSA-normalized polarization curves for HER in 0.05 M H_2SO_4. The commercial Pt/C benchmark catalyst exhibited excellent intrinsic activity with an overpotential of 30 mV at 10 mA cm^{-2} ECSA. Among the Co_2P catalysts, the single nanorod sample demonstrated the best activity with an overpotential of 400 mV (480 mV for nanorod bundles). This result reveals an important structure–activity relationship: while the nanorod bundle Co_2P possesses a substantially larger total ECSA (1.67 cm^2 *vs.* 1.28 cm^2), the single nanorod-decorated electrode exhibited higher intrinsic activity per active site. This suggests that the nanorod morphology preferentially exposes facets with superior catalytic properties for proton reduction in acidic media. The growth along specific crystallographic directions in the rod structure likely results in a higher density of active edge sites or specific surface terminations that facilitate efficient proton adsorption and H_2 evolution.

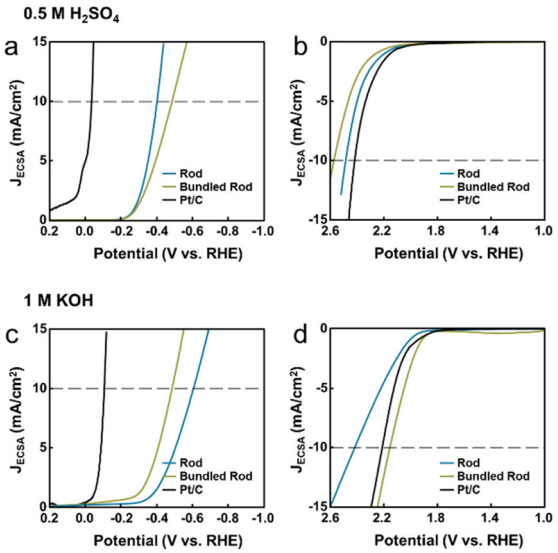

Fig. 4 (a) and (b) present experiments conducted in 0.5 M H_2SO_4, where (a) corresponds to HER activity and (b) to OER activity. (c) and (d) represent experiments performed in 1 M KOH, with (c) showing the HER and (d) showing OER performance. The catalyst in all cases is Co_2P: the olive color denotes the bundled rod morphology, blue represents the rod morphology, and black corresponds to a noble metal catalyst used for comparison.

In an alkaline electrolyte (Fig. 4c), the performance hierarchy shifts notably. The nanorod bundle Co_2P achieved 10 mA cm^{-2} for ECSA at an overpotential of 480 mV, compared to the single nanorod sample which required 600 mV. The commercial Pt/C catalyst showed an overpotential of 100 mV, confirming the substantial activity gap between precious and non-precious metal catalysts in the alkaline HER. The superior intrinsic activity of the nanorod bundle under alkaline conditions contrasts with the acidic conditions, suggesting fundamentally different rate-determining steps and active site requirements across pH regimes.

3.4.2. Oxygen evolution reaction (OER) activity. OER activity under acidic conditions (0.05 M H_2SO_4) was severely challenged for both morphologies (Fig. 4b). The nanorod bundle Co_2P exhibited an overpotential of 1.35 V at 10 mA cm^{-2} (ECSA: 2.55 cm^2), whereas the single nanorod Co_2P required 1.26 V (ECSA: 0.99 cm^2). The fact that the rod morphology demonstrates slightly superior intrinsic activity despite its substantially lower ECSA suggests enhanced stability of its active sites under harsh oxidative acid conditions. The reduced surface area of the rod structure likely minimises the total number of sites susceptible to oxidative degradation, phosphorus leaching, and structural collapse.

For OER activity in alkaline media (1 M KOH), as shown in Fig. 4d, the nanorod bundle Co_2P achieved 10 mA cm^{-2} at 0.46 V (ECSA: 2.13 cm^2), markedly outperforming the single nanorod sample, which required 0.62 V (ECSA: 1.90 cm^2). Its inferior performance indicates that the active sites presented by the bundled architecture are intrinsically more efficient for OER catalysis.

3.4.3. Structure–activity relationship and morphology-dependent performance. The morphology-dependent catalytic performance across different pH environments reflects differences in facet exposure, rate-determining steps, and structural stability.

In acidic HER, the superior activity of single nanorods despite lower ECSA is attributed to selective crystallographic facet exposure. One-dimensional rod structures preferentially expose edge sites and surface terminations that are thermodynamically favorable for proton adsorption and H_2 evolution.[31–33] The mixed exposure of various crystallographic planes in bundle structures results in reduced site-specific efficiency.

The performance reversal under alkaline conditions reflects a fundamental change in rate-determining steps. The superior performance of nanorod bundles can be attributed to two complementary effects. First, the high-curvature bundle architecture creates localized electric field amplification (the "lightning rod effect"), enhancing the electron injection efficiency at vertices and apex regions and facilitating efficient electron transfer during oxygen evolution.[34] Second, three-dimensional bundle structures enable faster oxygen bubble detachment, reducing diffusion overpotentials and improving the mass transport efficiency.[35]

In acidic OER, the superior activity of single nanorods despite lower ECSA reflects a tradeoff between surface area and oxidative stability. The reduced surface area minimizes sites exposed to harsh oxidizing conditions, mitigating phosphorus leaching. In acidic electrolytes, Co_2P undergoes rapid phosphorus dissolution as PO_4^{3-} or $H_2PO_2^-$ species, depleting active Co–P sites.[36] Rod structures, owing to their reduced surface area, expose fewer sites to this dissolution process, thereby preserving more catalytically active Co–P sites, compared to bundle structures which present a substantially larger surface for oxidative attack.

Rod-like structures favor selective facet exposure and oxidation resistance under acidic conditions, whereas bundle-like morphologies benefit from electric field enhancement and bubble evacuation kinetics under alkaline conditions. This structure–activity relationship highlights the critical importance of morphological engineering for catalytic performance optimization.

4. Conclusions

In this study, we experimentally demonstrated the precise control of the crystallinity, composition, and morphology of cobalt and nickel-based transition metal phosphide nanostructures using localized thermoelectrochemical synthesis. This strategy enabled the selective preparation of single-crystalline metal phosphides and diverse nanostructures that are challenging to achieve using conventional electrochemical deposition methods. Our approach provides a novel catalyst synthesis platform that optimizes structure and performance solely under electrochemical conditions without the need for

thermal annealing, while maintaining cost-effectiveness and procedural simplicity. Importantly, this methodology is extendable to a wide range of transition metal compounds, including selenides and sulphides, and is expected to make broad contributions to catalyst design in various energy conversion applications.

Author contributions

Hyokyum Ahn and Hyun S. Ahn designed the project. HyoKyum Ahn performed all experiments. Hyokyum Ahn and Hyun S. Ahn analyzed the results and wrote the manuscript. Yunwoo Nam and Taeyeon Kang contributed to data organization, storyline development, and visualization of the research findings.

Conflicts of interest

The authors declare no conflict of interest.

Data availability

The data supporting the findings of this study are provided in the main text and the supplementary information (SI). Supplementary information is available. See DOI: https://doi.org/10.1039/d5nr04780c.

Any raw data leading to the figures and tables are available upon reasonable request.

Acknowledgements

This work was supported by the Basic Science Research Program through the National Research Foundation (NRF) of Korea (RS-2024-00337549). Global—Learning & Academic Research Institution for Master's·PhD students, and the Postdocs (LAMP) Program of the NRF grant funded by the Ministry of Education (RS-2024-00442483). This work was also supported by the NRF grant funded by the Korea government (MSIT) (RS-2025-14383258).

This work was also supported by the Technology Innovation Program (20022479) funded by the Ministry of Trade Industry & Energy (MOTIE, Korea).

References

1 L. Fei, H. Sun, Y. Li, Y. Gu, W. Zhou and Z. Shao, *Energy Environ. Sci.*, 2025, **18**, 6456–6529.
2 J. Wei, Y. Shao, J. Xu, F. Yin, Z. Li, H. Qian, Y. Wei, L. Chang, Y. Han, J. Li and L. Gan, *Nat. Commun.*, 2024, **15**, 9012.
3 A. A. Feidenhans'l, Y. N. Regmi, C. Wei, D. Xia, J. Kibsgaard and L. A. King, *Chem. Rev.*, 2024, **124**, 5617–5667.
4 W. Moschkowitsch, O. Lori and L. Elbaz, *ACS Catal.*, 2022, **12**, 1082–1089.
5 H. Wang, Z. Yan, F. Cheng and J. Chen, *Adv. Sci.*, 2024, **11**, 2401652.
6 H. Zeng, Z. Chen, Q. Jiang, Q. Zhong, Y. Ji, Y. Chen, J. Li, C. Liu, R. Zhang, J. Tang, X. Xiong, Z. Zhang, Z. Chen, Y. Dai, C. Li, Y. Chen, D. Zhao, X. Li, T. Zheng, X. Xu and C. Xia, *Nat. Commun.*, 2025, **16**, 4314.
7 S. Jin, *ACS Energy Lett.*, 2017, **2**, 1937–1938.
8 A. Raveendran, M. Chandran and R. Dhanusuraman, *RSC Adv.*, 2023, **13**, 3843–3876.
9 T. Aziz, M. A. Haque, S. Saha, B. Mondal, S. Jain and A. Dutta, *Energy Fuels*, 2023, **37**, 18291–18309.
10 W. Zhang, N. Han, Y. Dou, X. Zhang, J. Luo, S. Dou and J. Fransaer, *ACS Catal.*, 2025, **15**, 5457–5479.
11 H. Yin, F. Rong and Y. Xie, *Int. J. Hydrogen Energy*, 2024, **52**, 350–375.
12 Y. Shi and B. Zhang, *Chem. Soc. Rev.*, 2016, **45**, 1529–1541.
13 J.-H. Chen, M.-F. Tai and K.-M. Chi, *J. Mater. Chem.*, 2004, **14**, 296–298.
14 A. E. Henkes and R. E. Schaak, *Chem. Mater.*, 2007, **19**, 4234–4242.
15 J. Wang, Q. Yang, Z. Zhang and S. Sun, *Chem. – Eur. J.*, 2010, **16**, 7916–7924.
16 C. A. Downes, K. M. Van Allsburg, S. A. Tacey, K. A. Unocic, F. G. Baddour, D. A. Ruddy, N. J. LiBretto, M. M. O'Connor, C. A. Farberow, J. A. Schaidle and S. E. Habas, *Chem. Mater.*, 2022, **34**, 6255–6267.
17 A. Shahmohammadi, S. Dalvand, A. Molaei, S. M. Mousavi-Khoshdel, N. Yazdanfar and M. Hasanzadeh, *RSC Adv.*, 2025, **15**, 13397–13430.
18 J. Kim, H. Kim, G. H. Han, S. Hong, J. Park, J. Bang, S. Y. Kim and S. H. Ahn, *Exploration*, 2022, **2**, 20210077.
19 N. Shida, J. A. Buss and T. Agapie, *Chem. Commun.*, 2018, **54**, 767–770.
20 C. Wang, Y. Wu, Z. Zhou, J. Wang, S. Pei and S. Liu, *Int. J. Hydrogen Energy*, 2022, **47**, 40849–40859.
21 W. Jo, D. Jeong, J. Jeong, T. Kim, S. Han, M. Son, Y. Kim, Y. H. Park and H. Jung, *Front. Chem.*, 2021, **9**, 781838.
22 Y. Lei, F. Lin, N. Hong, J. Zhang, Y. Wang, H. Ben, J. Li, L. Ding and L. Lv, *Materials*, 2023, **17**, 87.
23 M. W. Lee, J. H. Park, S. Cho and H. S. Ahn, *Small*, 2024, **20**, 2400038.
24 V. A. de la Peña O'Shea, P. R. de la Piscina, N. Homs, G. Aromí and J. L. G. Fierro, *Chem. Mater.*, 2009, **21**, 5637–5643.
25 W. Xu, Y. Li, T. Wu, Y. Duan, L. Zhu, Q. Liu, Y. Wang and W. Yu, *Materials*, 2025, **18**, 1747.
26 A. Brenner, D. E. Couch and E. K. Williams, *J. Res. Natl. Bur. Stand.*, 1950, **44**, 109.
27 M. M. Alsabban, M. K. Eswaran, K. Peramaiah, W. Wahyudi, X. Yang, V. Ramalingam, M. N. Hedhili, X. Miao, U. Schwingenschlögl, L.-J. Li, V. Tung and K.-W. Huang, *ACS Nano*, 2022, **16**, 3906–3916.
28 D.-H. Ha, L. M. Moreau, C. R. Bealing, H. Zhang, R. G. Hennig and R. D. Robinson, *J. Mater. Chem.*, 2011, **21**, 11498.

29 Y. Zhang, L. Gao, E. J. M. Hensen and J. P. Hofmann, *ACS Energy Lett.*, 2018, **3**, 1360–1365.
30 R. Himstedt, D. Hinrichs, J. Sann, A. Weller, G. Steinhauser and D. Dorfs, *Nanoscale*, 2019, **11**, 15104–15111.
31 J. Cai, Y. Song, Y. Zang, S. Niu, Y. Wu, Y. Xie, X. Zheng, Y. Liu, Y. Lin, X. Liu, G. Wang and Y. Qian, *Sci. Adv.*, 2020, **6**, eaaw8113.
32 M. Sheng, S. Fujita, S. Yamaguchi, J. Yamasaki, K. Nakajima, S. Yamazoe, T. Mizugaki and T. Mitsudome, *JACS Au*, 2021, **1**, 501–507.
33 Y. Men, P. Li, J. Zhou, G. Cheng, S. Chen and W. Luo, *ACS Catal.*, 2019, **9**, 3744–3752.
34 S. Sharma, N. Khatri, S. Puri, M. Adhikari, P. Wagle, D. N. McIlroy, A. K. Kalkan and Y. Vasquez, *ACS Appl. Mater. Interfaces*, 2024, **16**, 61858–61867.
35 J. Kim, S. Jung, N. Lee, K. Kim, Y. Kim and J. K. Kim, *Adv. Mater.*, 2023, **35**, 2370370.
36 A. Parra-Puerto, K. L. Ng, K. Fahy, A. E. Goode, M. P. Ryan and A. Kucernak, *ACS Catal.*, 2019, **9**, 11515–11529.